Radio Science

RESEARCH ARTICLE
10.1029/2020RS007235

Ionospheric Scintillation Data Inversion to Characterize the Structures Associated With a Series of Polar Cap Patches

James P. Conroy[1,2], Kshitija Deshpande[3], Bharat Kunduri[2], Roger H. Varney[4], Wayne Scales[2], and Amir Zaghloul[2]

[1]Johns Hopkins, Laurel, MD, USA, [2]Virginia Tech, Blacksburg, VA, USA, [3]Embry-Riddle, Daytona Beach, FL, USA, [4]SRI International, Menlo Park, CA, USA

Key Points:

- Inversion of Gloval Positioning System ionospheric phase scintillation data indicates that for this case study the irregularities associated with a series of Polar Cap Patches are predominantly composed of electron density rods that are elongated along the magnetic field that are in some instances interbedded between sheets and wings
- While wings and sheets of electron density irregularities can produce phase fluctuations, it is the apparent existence of rods that leads to higher values of phase scintillation
- The spatial and temporal distribution of the axial ratio (AXR) values also indicates that the measured phase fluctuations increase roughly proportionally with AXR values for rods but remain constant for wings and sheets

Correspondence to:
J. P. Conroy,
James.Conroy@jhuapl.edu

Citation:
Conroy, J. P., Deshpande, K., Kunduri, B., Varney, R. H., Scales, W., & Zaghloul, A. (2021). Ionospheric scintillation data inversion to characterize the structures associated with a series of Polar Cap Patches. *Radio Science*, *56*, e2020RS007235. https://doi.org/10.1029/2020RS007235

Received 2 NOV 2020
Accepted 4 JUN 2021

Abstract In this study, we present the results of an inversion of ionospheric phase scintillation data to characterize the plasma density irregularity parameters for the structures associated with a series of Polar Cap Patches. The parameter estimates obtained during the inversion suggests that the irregularities associated with Polar Cap Patches are predominantly composed of moderately elongated electron density rods aligned with the earth's magnetic field which in some instances are interbedded within sheet and wing like density structures. Analysis of the spatial and temporal distribution of the axial ratio (AXRs), which are the ratios of irregularity elongation parallel and perpendicular to the field, indicates that the measured phase scintillation indices increase roughly proportionally with AXR values for the rods but remain roughly constant for wings and sheets. These findings indicate that while wings and sheets can produce phase fluctuations, it is the apparent existence of rods that mark the occurrence of plasma processes that lead to the formation of field-aligned irregularities that produce phase scintillations which are most significant.

1. Introduction and Motivation

The ionosphere is a region above the earth extending from 90 to 1,000 km which is composed of weakly ionized plasma (Collin, 1985). As a radiowave propagates within the ionosphere, irregularities in the ionization can result in phase variations developing along the wave front through refraction and/or diffraction under weak scattering conditions (Yeh & Liu, 1982). The combination of these effects can induce random amplitude and phase fluctuations on a signal, otherwise known as scintillation, which can affect the ability of a receiver to close a link in the case of amplitude scintillation, or from reconstructing data symbols/bits in the case of phase scintillation. It is well known that ionospheric scintillation can severely impact the performance of space- and ground-based radar, communication, and navigation systems (Basu et al., 2002; Carrano, Groves et al., 2012; Humphreys et al., 2009; Kintner et al., 2007; Knepp, 2016; Knepp & Reinking, 1989). As arctic warming increases navigability in the polar latitudes (Marchenko, 2014), the impact of scintillation on Global Navigation Satellite System (GNSS) signals in these regions is an area of increasing importance. While advancements have been made over the years in works such as Deshpande et al. (2014, 2016); Jiao et al. (2013); Rino and Owen (1980), Rino et al. (1978); Wernik et al. (1990), there remains a need to better understand the structures and dynamics which produce scintillation for the purposes of forecasting, modeling, and to aid in the development of mitigation techniques. Our goals are to use a version of the model developed by Rino (1979) to perform an inversion on a relatively large set of Gloval Positioning System (GPS) data in order to gain new insight into the structures and dynamics of the irregularities associated with a series of patches.

Research into ionospheric scintillation has been ongoing for many years. The two general research areas are physics-based modeling and data-driven statistical analysis (Jiao et al., 2013). Physics-based modeling provides insight into the mechanisms that produce the characteristics of signals measured on the ground while data-driven analysis provides a comprehensive view of the occurrence and nature of scintillation on a large scale. Examples of physics-based modeling include Beach and Lovelace (1997), Briggs (1975), Carrano, Valladares et al. (2012), Deshpande et al. (2014), Knepp (1983), Lovelace et al. (1970), Rino (1979), and Rufenach (1974). Historically, scintillation research has largely focused on deepening our understanding of

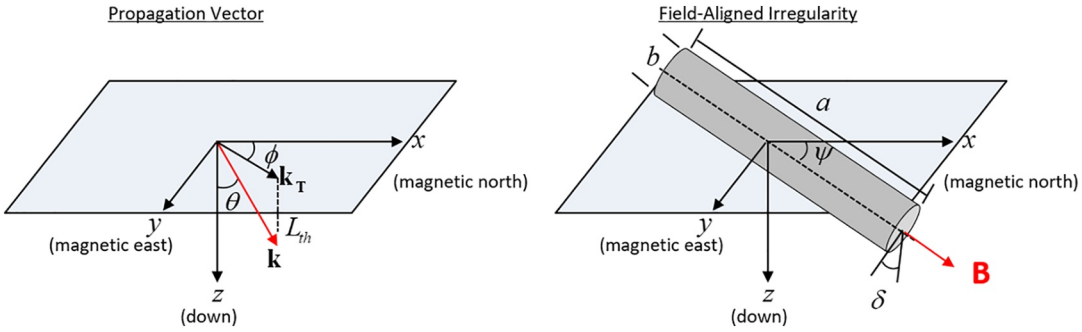

Figure 1. Propagation coordinate system, irregularity geometry, and magnetic field. Modified from Carrano (2012).

the equatorial region, where amplitude scintillations are predominant at GNSS frequencies (Aarons, 1982; Akala et al., 2012; Cervera & Thomas, 2006; Dandekar & Groves, 2004; Morton et al., 2014; Paznukhov et al., 2012). Research in the high latitude regions indicates that phase scintillation tends to occur more frequently than amplitude scintillations (Aarons, 1982; Jiao et al., 2013). Inversion papers include such classic works by Rino and Owen (1980); Rino et al. (1978); Wernik et al. (1990) and more contemporary works by Carrano, Valladares et al. (2012) and Deshpande et al. (2016). In this study, we identified a set of phase scintillation events which occurred during a minor geomagnetic storm as characterized by Planetary K-indexKp indices greater than four, and analyzed these events using data acquired by supporting ionospheric diagnostic measurements including high frequency (HF) radar, incoherent scatter rader (ISR), and the interplanetary magnetic field (IMF) readings. The events, which are interpreted as being associated with a series of Polar Cap PatchsPCPs, were then inverted in order to characterize the structures and dynamics using an analytic phase screen model. The inversion results are in good agreement with auxiliary instrument data and suggest that the composition of the irregularities associated with the PCPs were a mix of rods interbedded within sheet and wing-like electron density structures. Definitions for these structures are presented in Section 2.1.

The outline of this paper is as follows. Background information is presented Section 2. Details about the data and processing utilized in the study, the phase screen model, and the methodology used to perform the inversion are included in Section 3. The results of the inversion are presented in Section 4 along with a discussion. The conclusions are given in Section 5.

2. Background

2.1. Rods, Wings, and Sheets

The major electron density structures discussed in classic references such as Aarons (1982), Rino et al. (1978), Wernik et al. (1990), and in more contemporary references including Hosokawa et al. (2009) and Oksavik et al. (2015), consists of irregularities whose shapes can be characterized as either *rods*, *wings*, or *sheets*. In this work, rods, wings, and sheets are created using scaling factors along the axes of the electron density power spectral densities (PSDs) to dampen the contribution of smaller scale irregularities in preferential directions. The irregularity elongation scaling factor a is parallel to the magnetic field while b is perpendicular to the field. The rods are axially symmetric irregularities which are elongated along the earth's magnetic field with axis scaling factor a equal to 15, 10, and 5, and b equal to 1. For the sheets a and b were both equal to 5 or 10. For the wings a was set to 15 or 10 while b set to 5. A graphical representation of the irregularity geometry, propagation coordinate system and the magnetic field is included in Figure 1, where $\mathbf{k}$ is the principal propagation vector, $\mathbf{k_T}$ is the transverse spatial wavenumber, and δ and ψ are the magnetic declination and inclination respectively. The term Lth refers to the irregularity thickness, and a and b are the irregularity elongation factors with respect to the magnetic field vector $\mathbf{B}$. The dimensions of the irregularities and their PSD in the plane perpendicular to the line of sight dictate the scinitllation imposed on the propagating signal (Yeh & Liu, 1982). Additional details on the irregularity parameters and the angular dependence of the irregularity spectrum are given in Section 3.4 and Appendix A with the original derivation in Rino and Fremouw (1977).

2.2. Metrics

Scintillation is often characterized using the amplitude scintillation index (S_4), and the phase scintillation index (σ_ϕ). S_4 is the normalized standard deviation of the power which is given by

$$S_4 = \left(\frac{\langle P^2 \rangle - \langle P \rangle^2}{\langle P^2 \rangle} \right)^{1/2} \quad (1)$$

where P is the signal power. σ_ϕ is the standard deviation of the phase which is found as

$$\sigma_\phi = \left(\langle \phi^2 \rangle - \langle \phi^2 \rangle \right)^{1/2} \quad (2)$$

where ϕ is the signal phase after removing the geometric and static Total Electron Content (TEC) contributions, a process normally referred to as *detrending*. σ_ϕ is used in this work to identify ionospheric events for inversion.

2.3. Polar Cap Patches

Polar Cap Patches are F-region features of the ionosphere that appear as islands of high density, EUV-produced plasma, that can enter the Polar Cap through the Cusp dayside region of the Aurora, travel through the Cap region, and subsequently exit near midnight to return to the sunward flow patterns (Carlson, 2012; Crowley, 1996; Zhang et al., 2013). PCPs are often associated with severe TEC gradients (Jin et al., 2015) located along their edges, which can give rise to electron density irregularities through mechanisms such as the gradient drift instability (GDI) (Jin et al., 2015; Kelley et al., 1982; Lamarche & Makarevich, 2017). In addition it has also been noted that the apparent structuring within the patch itself can be associated with irregularities (Carlson, 2012). The irregularities associated with patches can lead to amplitude and phase scintillations (De Franceschi et al., 2008) which have been studied using GPS measurements (Jin et al., 2014). While there is no single agreed upon mechanism for patch generation (Carlson, 2012), previous research suggests that their existence is often correlated with southward values of the B_z component of the IMF (Hosokawa et al., 2009). It has also been observed in earlier observational work that the irregularities associated with patches are composed of rod field-aligned irregularities (FAIs) embedded within sheets (Hosokawa et al., 2009; Oksavik et al., 2015).

3. Data Sets and Model

3.1. Geophysical Activity

An examination of geophysical activity on November 6, 2015 is included in Figure 2. These data reveal an increase in geomagnetic activity from 18:30 to 20:30 Coordinated Universal Time (UTC), including Kp > 4, and Auroral Electrojet Index (AE) approaching ±15 nT. These values suggest that the high latitude regions were moderately disturbed during the time that the scintillation data were acquired. More importantly, IMF measurements from the Advanced Composition Explorer (ACE) satellite report B_z south from 18:00 to 24:00 UTC along with a significant increase in B_y. The change of B_z south approximately line up with the start of the scintillation events after accounting for the delay between the satellite and the ionosphere. These data suggest conditions which are favorable for the generation of PCPs in the Cusp (Hosokawa et al., 2009).

3.2. GPS

Scintillation events of interest were identified by processing and then analyzing data acquired by the Canadian High Arctic Ionospheric Network (CHAIN) high-rate Septentrio GPS receiver located at Arctic Bay (Jayachandran et al., 2009). Analysis was performed on data acquired at 50 Hz for 1.575 MHz (L1) center frequency. The processing of the raw data was completed as follows. Receiver clock jumps were first identified and then fixed using the method detailed in by Taylor et al. (2013). Once clock jumps were fixed, detrending was performed by filtering the raw carrier phase measurements, which were 60 s in length, using a high-pass sixth order Butterworth filter having a cutoff frequency of 0.1 Hz. S_4 values were then calculated using the standard deviation of the signal power normalized to the average power and the thermal noise

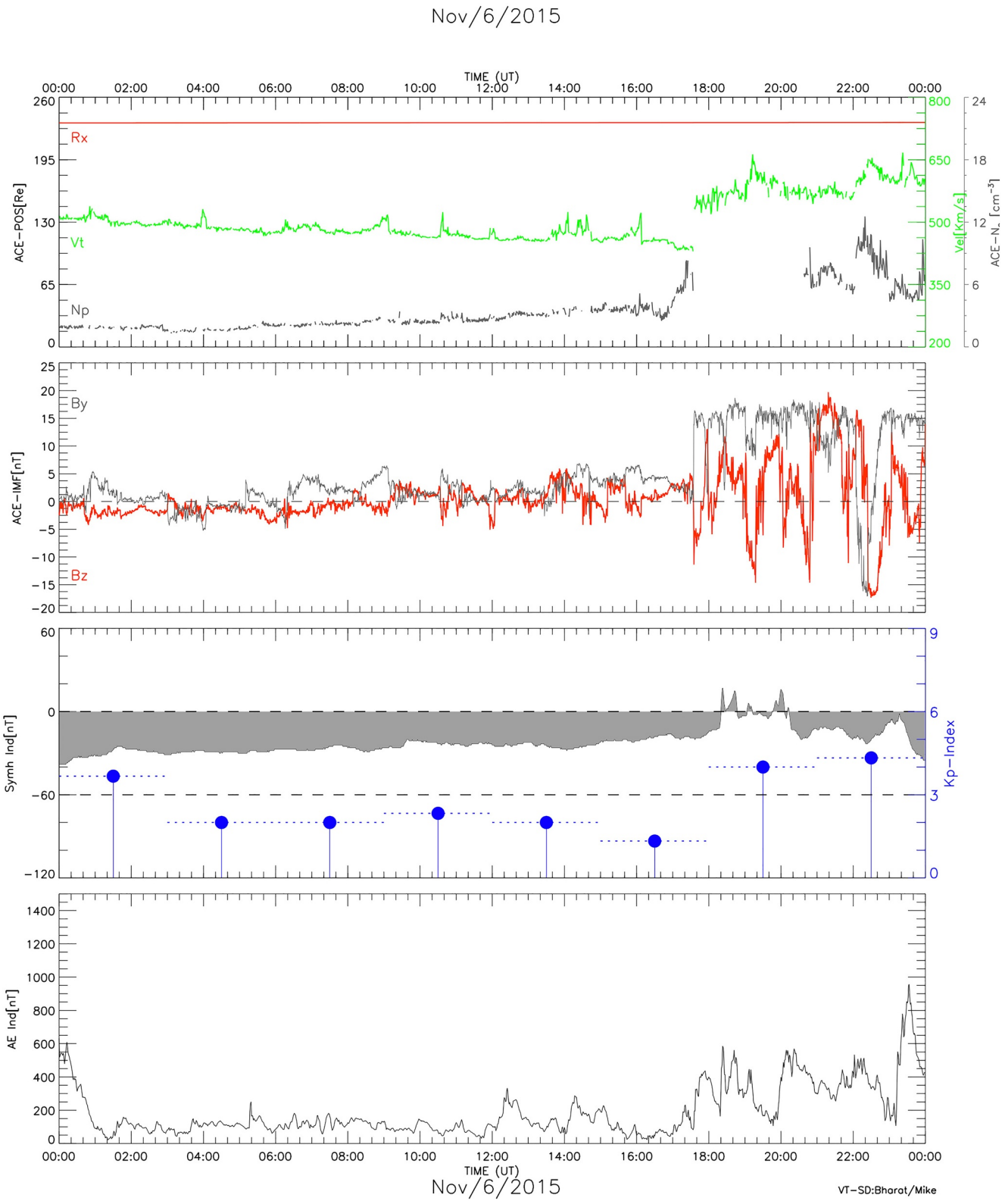

Figure 2. Geophysical activity plots including the solar wind, Kp, and AE data on November 6, 2015.

correction applied using the method presented in Dierendonck et al. (1993). σ_ϕ values were found using the standard deviation of the detrended carrier phase samples. In this work scintillation indices were calculated over 60 s in order to ensure the calculation of a robust statistic, and it was assumed that all geometric phase was removed by the detrending process without any aid from ephemeris data. An elevation mask of 30° was then used to minimize ground multipath as recommended by Jiao and Morton (2015) and Jiao et al. (2013). The geographic latitude and longitude of the Ionospheric Piercing Points (IPPs) were then calculated at an altitude of 300 km using the formula presented in Gaussiran et al. (2004). Calculated IPPs were then converted to geomagnetic latitude and longitude using the conversion given by Laundal and Richmond (2017). The UTC was converted to Geomagnetic Local Time (MLT) for the standard reference point 0°N, 0°E geographic latitude and longitude using the conversion presented by Baker and Wing (1989). The angle between the propagation path and magnetic field, defined in this work as the off-B Angle (OBA), was calculated at the IPPs using the magnetic field produced by the International Geomagnetic Reference Field (IGRF) model (Thébault et al., 2015).

3.3. Auxiliary and GPS Data Sets for Inversion

The data inversion was completed after carefully choosing GPS data near locations and during times where a range of auxiliary data were available to help estimate and/or bound the model input parameters. Auxiliary data included the Kp and AE indices, IMF measurements, Resolute Bay ISR, and Super Dual Auroral Radar Network (SuperDARN). Data selection began by identifying time segments where $\sigma_\phi > 0.15$ radians as prescribed by Jiao et al. (2013) in order to include only events that are considered to be noteworthy. Next, data was limited to OBA >35° in order minimize the number of propagation path's which are closely aligned to the magnetic field. This step was done as it has been found that the two-dimensional (2D) approximation, which the model hinges upon, becomes increasingly invalid for the longest irregularities as the angle between zenith and the earth's magnetic field approaches zero. Data were then limited to Geomagnetic Latitude (GMLT) >75°, from $-180° <$ to $< -30°$ Geomagnetic Longitude (GMLNG), and within the range of 9 and 15 MLT to provide a sufficient number of events in close proximity to the northern latitude SuperDARN sites. This process of down-selection led to the identification of a series of events acquired by the Arctic and Resolute Bay receivers on November 6, 2015 during 18:30 to 20:30 UTC. These data, which contained 283 scintillation measurements, were initially selected as they had IPPs in relatively close proximity to the ISR at Resolute Bay and were in the field of view (FOV) of two SuperDARN radar systems. A plot of the Arctic and Resolute Bay scintillation event IPPs measured from 18:30 to 20:30 UTC on November 6, 2015 with SuperDARN FOV plots from systems located at Rankin Inlet and Clyde River are included in Figure 3.

3.4. Phase Screen Model

A version of the power law phase screen ionospheric irregularity spectral model originally developed by Rino (1979) and used more recently by Carrano et al. (2016) was implemented to facilitate rapid inversion of ionospheric scintillation data for irregularity parameter estimation. While the emphasis of this work is the use of this model as a tool to aid in the rapid inversion of a large data set a full description and accounting of each model parameter is included in Appendix A. The model utilizes the classic approximation developed by Rino and Fremouw (1977) to reduce the three-dimensional (3D) electron density PSD to the 2D phase PSD in the plane perpendicular to the propagation path. The 2D phase PSD is of the form

$$\Phi_\phi(\mathbf{K}) = \frac{abC_p}{(K_0^2 + AK_x^2 + BK_xK_y + CK_y^2)^{(p+1)/2}} \tag{3}$$

where p is the phase spectral index, $K_0 = 2\pi/L_0$ is the wavenumber of the outer scale L_0, and a and b are irregularity elongation scaling factors operating parallel and perpendicular to the magnetic field as defined in Figure 1. A, B, and C are dependent on the direction of propagation and the orientation of the magnetic field and are found by relating the line of sight and the irregularity axes. The horizontal irregularity wavenumbers along geomagnetic north and east are K_x and K_y. The strength of the 2D PSD of the phase is driven by the factor C_p which in practice is evaluated at 1 rad/m. C_p is a complicated function of parameters including the propagation signal wavelength in free space λ, the thickness of the irregularity layer Lth, zenith angle

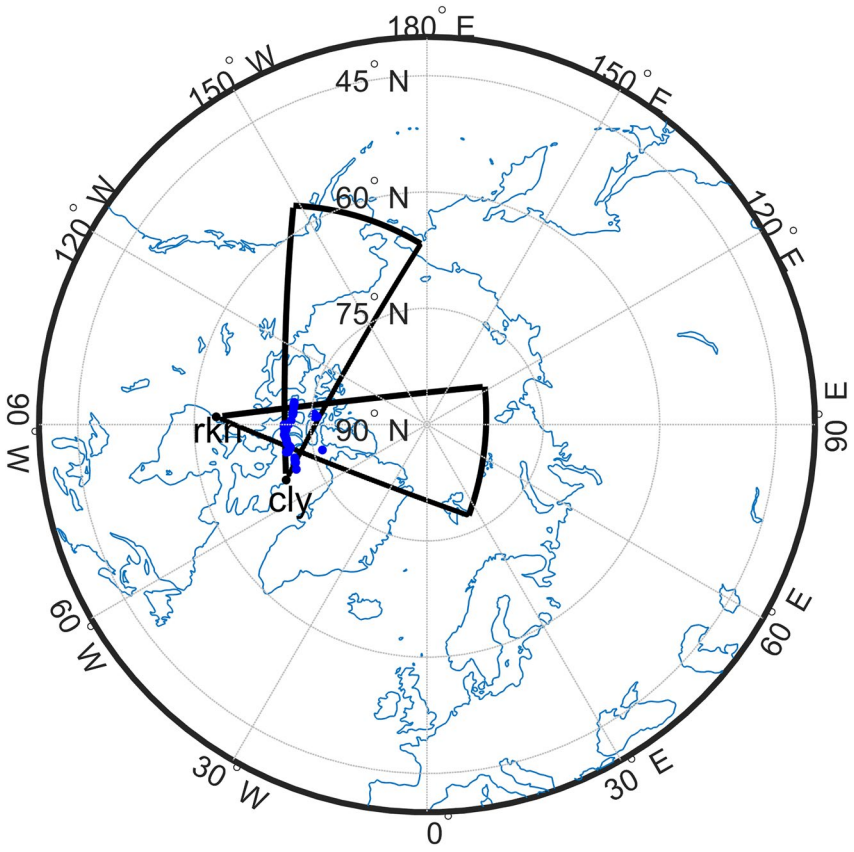

Figure 3. Arctic and Resolute Bay scintillation event IPPs measured (blue dots) from 18:30 to 20:30 UTC on November 6, 2015 with SuperDARN FOV plots from systems located at Rankin Inlet and Clyde River.

θ, the variance of the electron density ΔN_e^2, the outer scale cutoff wavenumber and the 3D spectral index ν. Equation 3 can be manipulated to find a compact expression for the one-dimensional (1D) PSD of the phase signal on the ground as

$$\phi(f) = \frac{T}{\left(f_0^2 + f^2\right)^{p/2}} \tag{4}$$

where f and f_0 are temporal frequencies, T is the 1D spectral strength given by Equation A7, and p is the 1D spectral index. T, which is typically sampled at 1 Hz, is also dependent on a host of parameters such as C_p, p, propagation geometry, irregularity orientation and elongation, along with satellite and plasma velocities. Equation 4 was used in this work to support the inversion.

3.5. Method of Inverse Modeling

In this section, we give an overview of the inverse modeling approach. The objective of the inversion is to fit model outputs to the observed data to derive the optimal values of the model input parameters. The model input parameters are presented in Table 1.

For each inverse modeling run, there are nine unknown parameters, shown in Table 1 in boldface. These unknown parameters are found by completing a multiple step inversion process summarized below. For every data observation, the geographical parameters, including the magnetic declination (δ) and inclination (ψ) at the Ionospheric Piercing Point (IPP), and azimuth and elevation of the propagation vector, are obtained using the IGRF model and the Standard Product 3 GPS Format (sp3) trajectory.

Table 1
Model Input Parameters

Input	Note
$\mathbf{L_o}$	The outer scale
P	Spectral index
$\mathbf{\Delta N_e}$	Root-mean-square (RMS) electron density fluctuations
a	Irregularity elongation scaling factor parallel to the magnetic field
b	Irregularity elongation scaling factor perpendicular to the magnetic field
$\boldsymbol{L_{th}}$	Irregularity layer thickness
$\boldsymbol{h_{irreg}}$	Irregularity layer altitude
$\mathbf{\lvert V_d \rvert}$	Irregularity drift velocity magnitude
$\mathbf{V_d\angle}$	Irregularity drift velocity angle measured from magnetic north
δ	Magnetic declination
Ψ	Magnetic inclination
LOS(*Az*, *El*)	LOS azimuth and elevation

Note. Unknown quantities are highlighted in bold.

Initially, for each GPS observation, the auxiliary data is used to estimate the values of as many input parameters as possible. The details of this step are included in Section 3.5.1. In order to further reduce the dimensions of the parameter space, values for some of the other input parameters, including the outer scale (L_o), AXR defined as a/b, and the irregularity thickness (L_{th}) are assumed. The outer scale is the largest spatial scale of the irregularities, while the AXR defines the anisotropy of the FAIs. The remaining four free parameters include ΔN_e (assuming a constant Lth), p, and drift irregularity drift velocity magnitude ($|V_d|$) and angle ($V_d\angle$). The values of each of the parameters used in the inversion are presented in Section 3.5.1. The turbulence strength T is a function of ΔN_e given in electrons per cubic meter and the irregularity layer thickness (L_{th}), and is often expressed in TEC units (TECU, 1 TECU = 10^{16} el/m^2). The magnitude of the phase PSD is proportional to the turbulence strength (Deshpande et al., 2014; Rino & Fremouw, 1977; Wernik et al., 1990). The effective drift velocity V_{eff}, which is derived from the geometry, impacts the magnitude of the phase fluctuations as a function of temporal frequency. Finally, the spectral index p largely dictates the shape of the PSD as a function of frequency. As detailed in Section 3.5.2, the remaining input parameters are estimated from the best fit of the simulated PSD to the measured PSD by completing a series of models over a uniform four-dimensional (4D) grid that defines the remaining parameter space.

3.5.1. Step 1: Use of Auxiliary Data

Data from the auxiliary instruments were analyzed in order to reduce the parameter space to 4D and to bound the range of input values. A series of PCPs, in the F-region of the ionosphere, were observed in the ISR data and have an estimated thickness and altitude of 100 and 300 km respectively. However, it was found that most of the IPPs of the scintillation events occurred approximately 1° GMLT to the south of the ISR FOV in the area of the electron density gradient associated with the patches. The irregularities were therefore assumed to be associated with gradient drift instabilities. Furthermore, since the irregularities associated with high-latitude scintillations are often considered to be relatively thin (Deshpande et al., 2014), especially when compared to a PCP, the inversion was run with Lth and altitude irregularity layer altitude (h_{irreg}) equal to 40 and 300 km, respectively. The $|V_d|$ and $V_d\angle$ was approximated for each scintillation measurement using SuperDARN convection velocity data which was compiled from data acquired by multiple systems. However, given the inherent uncertainty of using velocities estimated from SuperDARN data, the inversion was run for the velocity derived at each IPP ± 100 m/s. The outer scale (L_o) was set to 2 km, which according to Yeh and Liu (1982) is the approximate cutoff scale for irregularities associated with significant phase scintillation, and the spectral index (p) was swept from 1 to 5. The propagation frequency was the L1 GPS signal. The RMS electron density fluctuations (ΔN_e) was 0.05×10^{11} to 1×10^{12} el/m^3.

3.5.2. Step 2: Uniform Grid Simulation

The simulations were run over a 4D grid for set of discrete AXR values. The 4D grid included ΔN_e, p, $|vd|$, and $vd\angle$. The ΔN_e and p grids were created from vectors with 80 values. The $|vd|$ grid was composed of the $|vd|$ measured by SuperDARN at the IPP for the event ±100 m/s, with an interval of $\Delta|vd| = 50$ m/s The $vd\angle$ values were created using the measured velocity azimuth with an interval of $\Delta vd\angle = 10°$ The axis scaling factors were chosen to simulate irregularities that can be characterized as either *rods*, *wings*, or *sheets*. These basic shapes were chosen since these are the major structures discussed in classic references such as Aarons (1982), Rino et al. (1978), Wernik et al. (1990) and in more contemporary references including Hosokawa et al. (2009) and Oksavik et al. (2015). The rods are modeled as axially symmetric irregularities which are vertically elongated and parallel to the earth's magnetic field with axis scaling factor a equal to 15, 10, and 5, and b equal to 1. For the sheets a and b were both equal to 5 or 10. For the wings a was set to 15 or 10 while b set to 5. In considering solutions for each scintillation event, a least squares approach as detailed in Press et al. (1992), was utilized to evaluate the goodness of fit of each model variant using the same approach used by Carrano and Rino (2019), Carrano, Valladares et al. (2012), and Deshpande et al. (2016). For this work the following cost function was used

$$\chi^2 = \frac{1}{\sigma_y^2}\sum_{i=1}^{N}\left(\log_{10} Y_i - \log_{10} X_i\right)^2 \tag{5}$$

where N is the number of measurements, Y is the modeled PSD and X is the measured spectrum. For a good fit it is required that $\chi^2 \approx (N - M)$ or $\chi' = \chi^2/(N - M) \approx 1$. $(N - M)$ is the degrees of freedom and M is the number of unknown variables. In this study the N was set equal to 469 and M is 4.

4. Results and Discussion

The scintillation events, which are interpreted as being created by irregularities associated with a series of PCPs, were inverted in order to characterize the underlying structures using an analytic phase screen model. Analysis of the inversion results and auxiliary measurements is included in the following section along with a discussion.

4.1. ISR

Resolute Bay North incoherent scatter radar (RISR-N) measurements of electron density, temperature, and velocity acquired during the time period of interest are included in Figure 4. During this event RISR-N used an 11-beam mode interleaving 330 μs uncoded long pulses with 480 μs 16-baud alternating code sequences. The processing of these data included the generation of autocorrelation functions from the two different types of pulses which were fit for plasma parameters at 24 and 4.5 km range resolution, respectively. Then, the vector velocities were reconstructed from the long pulse line-of-sight velocities using the algorithm described by Heinselman and Nicolls (2008). Inspection of these data reveal the existence several significant electron density structures which overlap in time with the scintillation events. The first structure, which begins shortly after 18:30 UTC and continues until approximately 18:40 UTC, is interpreted as a flow channel given the high plasma velocity in the poleward direction, rise in ion temperature, and apparent electron density void which has been created. Large ion-neutral velocities differences elevate the ion temperature via frictional heating (Thayer & Semeter, 2004), and the elevated ion temperatures accelerates the F-region recombination leading to a density cavities (Zettergren et al., 2015). The next set of structures are a series of PCPs, with their characteristic increase in electron density, which begin at approximately 18:40 UTC and continue until 19:25 UTC. The PCPs, which appear to be constructed out of vertically elongated electron density features, have an electron density of approximately 8×10^{11} el/m^3, are centered at an altitude of around 300 km, and are roughly 100 km thick. The third structure is a Polar Arc, which begins abruptly at 19:25 UTC and lasts for about 5 min, and has resulted in a significant increase in electron density between 110 and 140 km altitude. Finally, there is another PCP observed at 20:15 UTC, which has an altitude and thickness which is comparable to the previous patches.

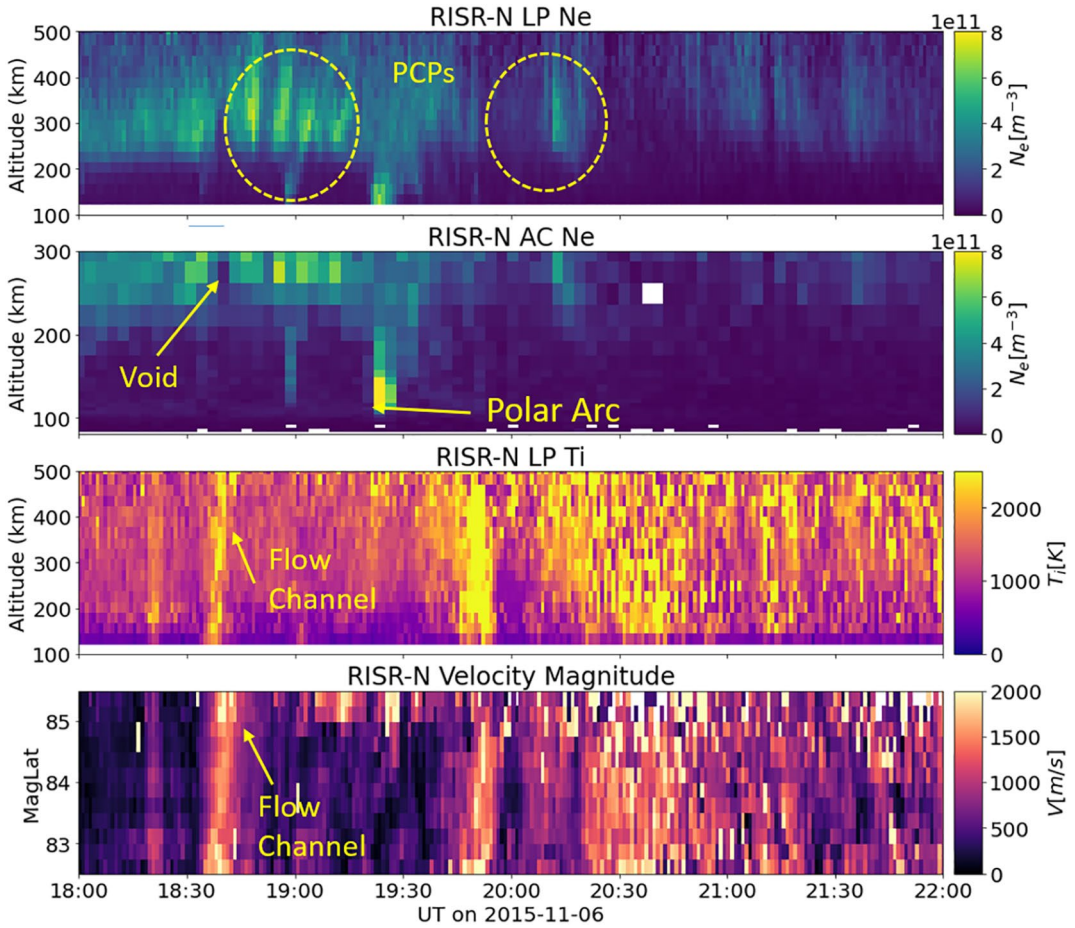

Figure 4. The panels include data acquired by the RISR-N system on November 6, 2015, which show (a) Electron density from the power in the long pulses without a temperature correction, (b) Fitted and temperature-corrected electron density from the alternating codes, (c) Ion temperature from the long pulses, and (d) The magnitude of the reconstructed vector velocities. Panels (a)–(c) show the data from beam 64,280, which has an azimuth which is 26° east of geographic north, and an elevation of 75° above the horizon.

4.2. SuperDARN

SuperDARN data acquired by the Rankin Inlet system was analyzed for the time period of interest and are included in Figure 5. An examination of the backscattered power demonstrates the existence of complex FAIs whose slant range approximately overlaps the IPPs of the scintillation events. The velocity measurements suggest apparent plasma velocities which are predominately greater than 600 m/s. A closer look at the TEC data indicates slant-range-dependent TEC which is consistent with the existence of electron density gradients between the SuperDARN system and the IPPs. During the inversion, merged convection velocity data compiled from data acquired by multiple SuperDARN systems were used to seed the $|V_d|$ and $V_d\angle$ estimates for each scintillation measurement. A plot of the ISR beams acquired during the experiment along with the IPPs and a time snapshot of the SuperDARN-derived convection velocity is included in Figure 6.

4.3. Inversion Results

In this section we present the results of the data inversion and irregularity parameter estimation. The data inversion was performed over all the scintillation data acquired from 18 to 22 UTC, for each parameter combination, and the optimal solution was estimated by determining the solution with the χ' that was closest to unity. An example of the results obtained for a single case is included in Figure 7, which shows a slice of

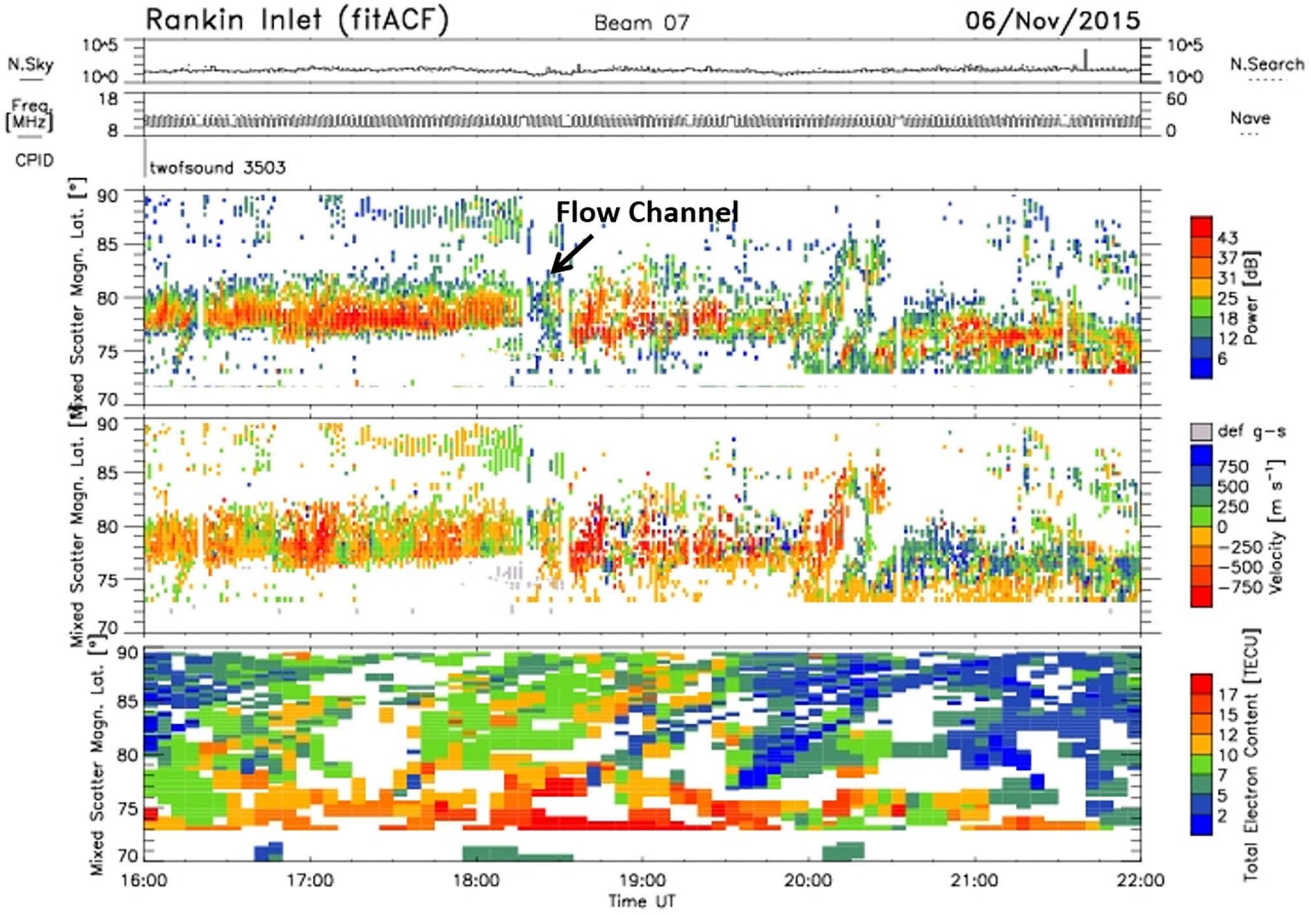

Figure 5. SuperDARN data acquired by the Rankin Inlet radar. Courtesy of the University of Saskatchewan.

the χ' values obtained for the 4D parameter space exercised in this instance. In this case it was found that the optimal solution was obtained for a and b equal to 10, a value of p approaching 3, and a moderate ΔN_e of 3.6×10^{11}(el/m^3). The measured and modeled PSD for this case is included in Figure 8. By inspection, these results demonstrate that with the optimal irregularity parameters estimated for this case, a reasonable fit is obtained between the model and the measured data. A closer look at the contour data in Figure 7 reveals that the contour level associated with χ' values approaching unity, namely 1.1794 in this case, is relatively large. These results indicate that the PSD and measurements can be matched relatively well over a relatively wide range of ΔN_e and p values, due to the high amount of variation observed in the PSD for frequencies greater than 1 Hz.

A plot of the spatial and temporal distribution of the AXR of the irregularity estimates is included in Figure 9, where the data marker values have been scaled by the measured phase scintillation indices so that symbol size is proportional to $100 \times \sigma_\phi$. These results indicate that longer AXR values are associated with higher measured phase scintillation indices. They also show that for structures which are characterized as wings and sheets, that phase scintillation values are relatively constant. These findings illustrate that while wings and sheets can produce phase fluctuations to be measured by the receiver, that it is the apparent existence of rods that mark the occurrence of plasma processes that give rise to the FAIs that lead to more severe phase scintillation. These results also indicate that while the irregularities are predominantly composed of elongated rods, there are several instances where rods are found to be interbedded between sheets and wings. Furthermore, in some instances it is observed that the occurrence of sheets or wing marks the beginning and end of a series of phase scintillation events and/or the transition between cases of higher to lower AXR. While these data only suggest that a pattern may be present in the formation

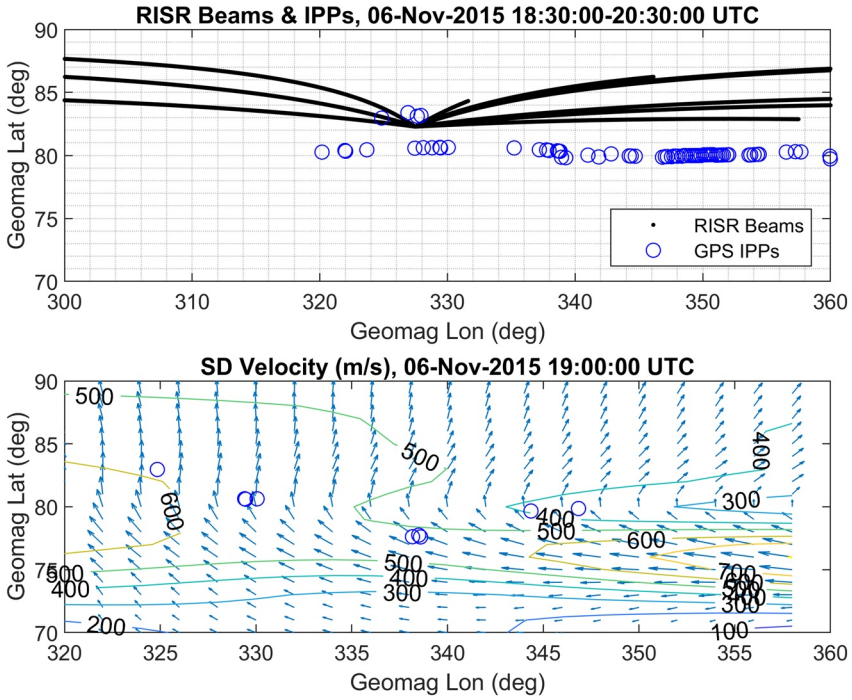

Figure 6. ISR beams acquired during the experiment along with the IPPs and a time snapshot of the SuperDARN-derived convection velocity.

and modification of ionospheric irregularities, a crude parametric study performed on data realizations produced for rods tells us that while there can be an ambiguity in the solution as a function of propagation angle, that when considering a range of angles, as was done in this work, that our method will yield

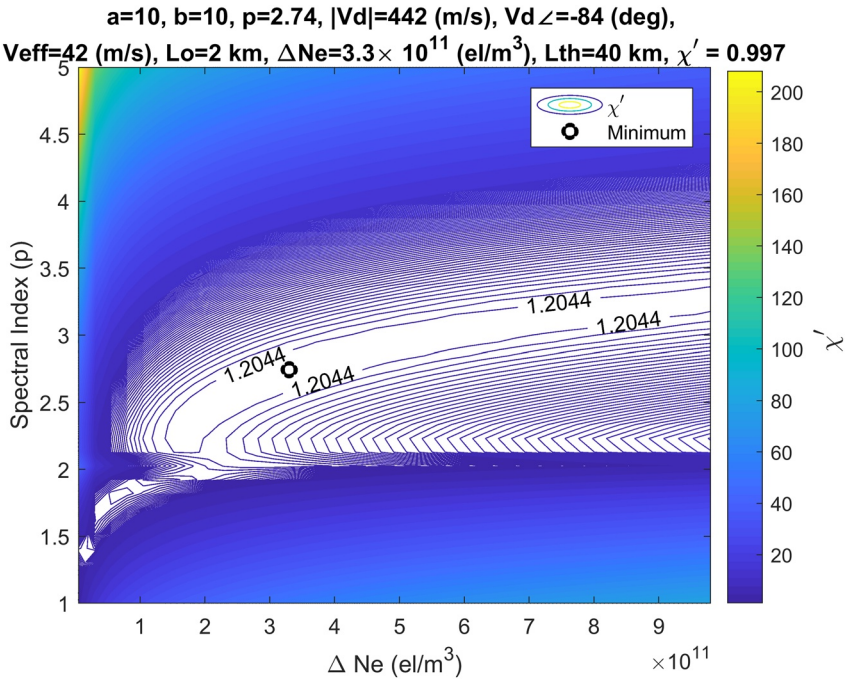

Figure 7. A contour plot of χ', which shows a slice of the solutions obtained for the 4D parameter space as a function of ΔN_e and p, along with the minimum χ' value for the optimal drift velocity, a and b, for 60 s of GPS scintillation data acquired on November 6, 2015 beginning at 18:11:30 UTC.

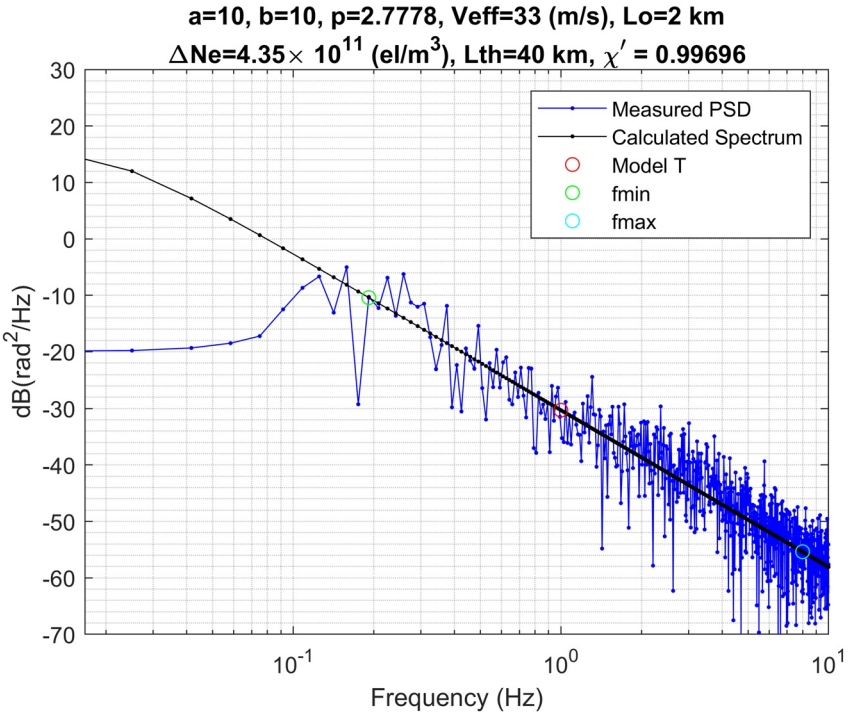

Figure 8. PSD of the model and measured data for 60 s of GPS phase scintillation data acquired on November 6, 2015 beginning at 18:11:30 UTC. PSD, Power spectral density.

results which are consistent with the physical structure under consideration. An exhaustive parametric study and an examination into the physical basis and rate of occurrence for the generation of irregularities will be left for future work.

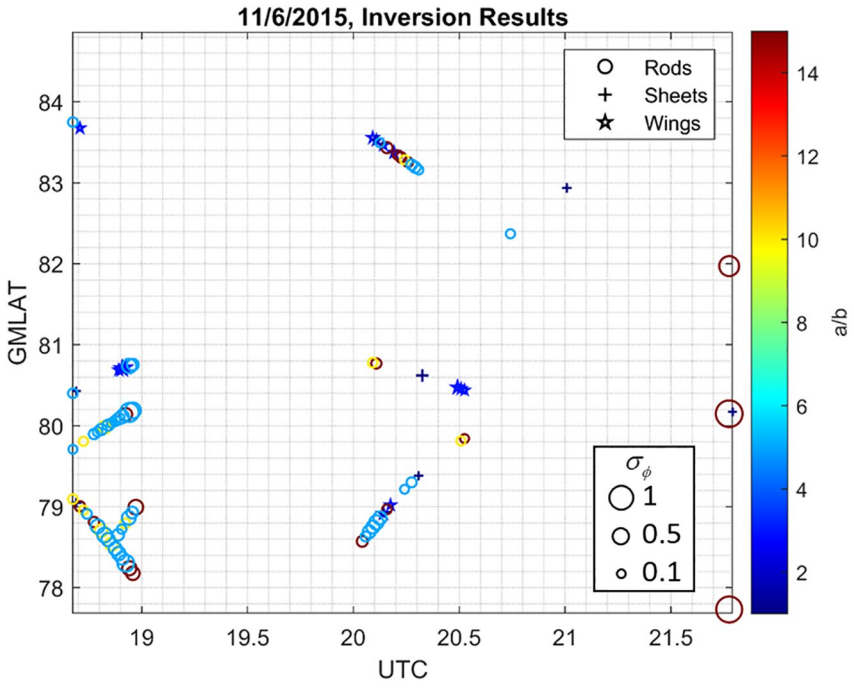

Figure 9. Spatial distribution of inversion solutions for GPS scintillation data acquired on November 6, 2015 from 18:00 to 22:00 UTC. Marker values have been scaled by $100 \times \sigma_\phi$. GPS, Gobal positioning system.

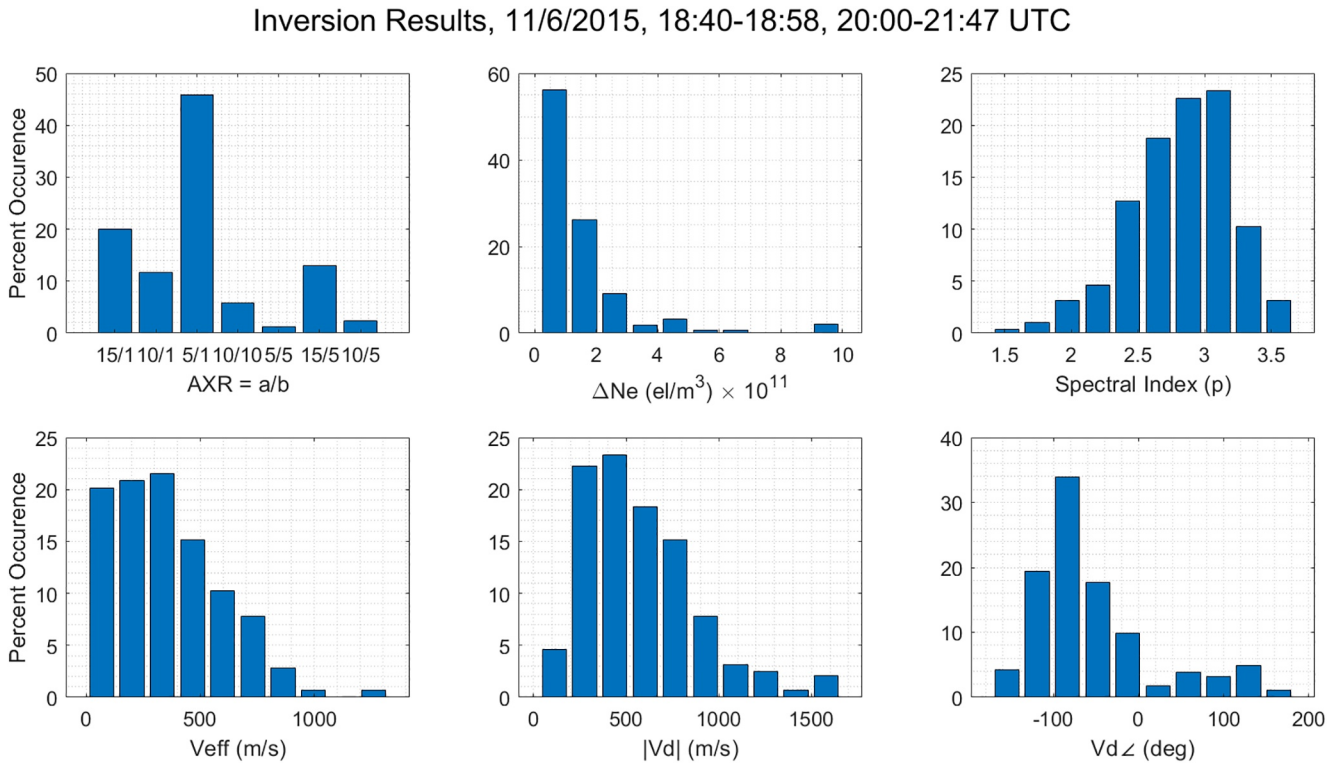

Figure 10. Histograms of irregularity parameters estimates for the optimal inversion solutions.

Once, a reasonable solution was obtained for all of the scintillation events, the data were down-selected as a function of time, using the auxiliary data as guidance, in an effort to focus on the irregularity parameters associated with the existence of PCPs. Using the ISR data in Figure 4 and SuperDARN data in Figure 5, the channel flow was estimated to exist from ~18:15 to 18:40 UTC, after which the PCPs became predominant until the arc was observed by the ISR at ~19:25–19:30 UTC. Unfortunately, there is no direct evidence for the Polar Arc in the SuperDARN data as the center frequency was not tuned to be sensitive to irregularities at such low altitudes. However, the convection vector velocity estimates during this time had a magnitude which was predominantly greater than 600 m/s with a general north-west sense of direction. Considering that the geographic arc length between the ISR and Arctic Bay is approximately 415 km, a convection velocity which is east-west at 600 m/s would provide roughly 12 min between the time that the arc would have presumably been over Arctic Bay until it reached the ISR. With this in mind, and taking into account the uncertainty in the convection velocity estimates and their presumed influence on the location of the arc, the PCPs were presumed to exist in the region of the scintillation receiver between 18:40 and 19:00 UTC and again after 20:00 UTC. Down-selection using these parameters resulted in the number of scintillation events being reduced to 85 that were statistical analyzed in an effort to obtain insight into trends observed in the inversion results. A series of histograms of the optimal irregularity parameters is presented in Figure 10. These results indicate several interesting things about the structure of the ionosphere over the duration of the scintillation events associated with the existence of the PCPs. It is clear from these data that the irregularities were largely composed of rods with moderate vertical elongation as an AXR of 5 is obtained for approximately 45% of the events. Solutions with an AXR of 15 are also observed for about 20% of the cases which indicates the presence of longer rod-shaped irregularities a significant percentage of the time. Sheets and wings are also observed for around 16% of the solutions. Collectively, these results suggest the predominance of FAIs irregularity structures which is consistent with those observed by the SuperDARN data. The distribution of the p estimates indicates that ~85% of the solutions have p between 2.4 and 3.2, with 2.7 being the most predominant, while the solutions for the RMS of the electron density fluctuations suggest that overall the magnitude is quite modest with a value of $1 \times 10^{11}(\mathrm{el/m^3})$. Turning our attention to v_d and effective velocity ($|V_{\mathrm{eff}}|$) solutions reveal the importance of properly accounting for the satellite geometry effects.

V_{eff}, which is the effective scan velocity, relates the propagation geometry and the irregularity drift velocity vectors to give the effective velocity along the line of sight (see Appendix A for more details). In the results the probability mass of V_{eff} are primarily limited to 800 m/s or less while the estimated v_d is mostly found for values as high as 1,100 m/s. It is observed that the majority of the effective velocities are between 70 and 460 m/s while the drift velocities are between 310 and 630 m/s. The angles of the drift velocities are predominantly west-to-northwest of magnetic north which overall is consistent with the SuperDARN observations.

5. Conclusions

In this study, we presented the results of an inversion of phase scintillation data to estimate irregularity parameters of the structures associated with PCPs. Analysis of the irregularity parameter estimates obtained by inverting the scintillation data associated with a series of PCPs suggest that the irregularities are predominantly composed of moderately elongated rods interbedded within sheet and wing like structures. These structures, which generally have a spectral density between 2.4 and 3.2 and modest (ΔN_e) values on the order of 1×10^{11}(el/m^3) have $|V_{\text{eff}}|$s between 70 and 460 m/s oriented predominantly west-to-northwest of magnetic north. The spatial and temporal distribution of the AXR values also indicates that the measured σ_ϕ increase roughly proportionally with AXR values for the rods but remain approximately constant for wings and sheets. While attributing these findings to a particular type of plasma instability is beyond the scope of this study and will be left for future work, these results indicate that while wings and sheets can produce phase fluctuations, it is the apparent existence of rods that marks the occurrence of plasma processes that give rise to the FAIs that lead to more severe phase scintillations. Finally, our results show several instances where rods are found to be interbedded between sheets and wings, and that the occurrence of sheets or wing may mark the beginning and end of a series of phase scintillation events and/or the transition between cases of higher to lower AXR.

Appendix A: Analytic Phase Screen Model

A version of the power law phase screen ionospheric irregularity spectral model originally developed by Rino (1979) is included in this Appendix along with explicit definitions of all the terms for reference purposes. The model utilizes the classic approximation developed by Rino and Fremouw (1977) to reduce the 3D electron density PSD to the 2D phase PSD in the plane perpendicular to the propagation path. The 2D phase PSD is of the form

$$\Phi_\phi(\mathbf{K}) = \frac{abC_p}{(K_0^2 + AK_x^2 + BK_xK_y + CK_y^2)^{(p+1)/2}} \tag{A1}$$

where p is the phase spectral index, $K_0 = 2\pi/L_0$ is the wavenumber of the outer scale, and a and b are irregularity elongation scaling factors operating parallel and perpendicular to the magnetic field (Figure 1). A, B, and C are the dependent on the direction of propagation and the orientation of the magnetic field and are found by relating the line of sight and the irregularity axes. The horizontal irregularity wavenumbers along geomagnetic north and east are K_x and K_y. C_p, which is the strength of the 2D PSD of the phase evaluated at 1 rad/m, is found using

$$C_p = r_e^2\lambda^2 C_s L_{th}\sec\theta \tag{A2}$$

where r_e is the electron radius $\left(2.8179 \times 10^{-15} m\right)$, λ is the wavelength in free space, L_{th} is the thickness of the layer, and θ is the zenith angle. C_s is given by

$$C_s = 8\pi^{3/2}\langle\Delta N_e^2\rangle K_0^{2\nu-2}\Gamma\left(\nu + 1/2\right)/\Gamma\left(\nu - 1\right) \tag{A3}$$

where ΔN_e^2 is the variance of the electron density, $\langle\rangle$ is the ensemble average, and ν, the 3D spectral index is approximately equal to $p/2$. For this model, S_4, which is valid for $1 < p < 5$, can be calculated as

$$S_4^2 = C_p\rho_F^{p-1}F_s\left(p\right)\wp\left(p\right) \tag{A4}$$

where $\rho_F^2 = z\sec\theta / k$ is the Fresnel scale, z is the height of the layer, and k is the free space wavenumber of the propagating signal. The term $F_s(p)$ is found as

$$F_s(p) = \frac{\Gamma\left[(5-p)/4\right]}{2^{(p-1)/2}\sqrt{\pi}(p-1)\Gamma\left[(p+1)/4\right]} \tag{A5}$$

while $\wp(p)$ is a factor which accounts for the propagation geometry and is defined in Equation A24. The 1D phase power spectral density can be found as

$$\phi(f) = \frac{T}{\left(f_0^2 + f^2\right)^{p/2}} \tag{A6}$$

where f are the temporal frequencies calculated using the effective velocity (V_{eff}, Equation A12) and spatial wave numbers, and f_0 is found as $f_0 = V_{\text{eff}}/L_0$. The 1D spectral strength sampled at 1 Hz is

$$T = C_p F_t(p) G V_{eff}^{p-1} \tag{A7}$$

where G is the phase enhancement factor due to the geometry (Rino, 1979). V_{eff} is the effective scan velocity, which relates the spatial scale of the structures along the satellite path, to the corresponding frequency in the temporal domain. The equation for $F_t(p)$ is given by

$$F_t(p) = \frac{\sqrt{\pi}\Gamma\left[p/2\right]}{(2\pi)^{p+1}\Gamma\left[(p+1)/2\right]} \tag{A8}$$

σ_ϕ, which is the standard deviation of the phase of the signal, is related to the two-sided temporal PSD by

$$\sigma_\phi^2 = \int_{-\infty}^{\infty} \frac{T}{\left(f_0^2 + f^2\right)^{p/2}} df \tag{A9}$$

Given that we are typically interested in the phase pertubation on signals after the removing low frequency phase shifts due to the geometric propagation path length and TEC, σ_ϕ^2 can be related to the one-sided temporal PSD by

$$\sigma_\phi^2 \approx 2T \int_{\tau_c^{-1}}^{\infty} f^{-p} df = \frac{2T}{p-1}\tau_c^{p-1} \tag{A10}$$

where τ_c is the time constant of the detrend filter and it is assumed that $\tau_c \ll L_0/V_{\text{eff}}$. Applying A7–A10 yields a compact expression for σ_ϕ^2

$$\sigma_\phi^2 = \frac{2}{p-1} C_p F_t(p) G\left[\tau_c V_{eff}\right]^{p-1} \tag{A11}$$

The effective scan velocity V_{eff} is related to the propagation geometry and the irregularity drift velocity vectors by the expression

$$V_{eff} = \sqrt{\frac{CV_{sx}^2 - BV_{sx}V_{sy} + AV_{sy}^2}{AC - B^2/4}} \tag{A12}$$

V_{sx} is the magnetic northward component of the plasma velocity relative to the raypath scan velocity at the IPP and is given by

$$V_{sx} = V_{dx} - V_{px} - \tan\theta\cos\phi V_{pz} \tag{A13}$$

V_{sy} is the magnetic eastward component of the plasma velocity relative to the scan velocity of the raypath at the IPP and is found using

$$V_{sy} = V_{dy} - V_{py} - \tan\theta \sin\phi V_{pz} \tag{A14}$$

where θ is the nadir angle at the IPP, ϕ is the magnetic meridian angle of the propagation vector, and V_{dx} and V_{dy} are the plasma drift velocity vectors in the magnetic north and east directions, respectively. V_{px}, V_{py}, and V_{pz} are the magnetic northward, magnetic eastward, and downward components of the raypath velocity at the IPP. The coefficients required for Equation Appendix A

$$A = C_{11} + C_{33}\tan\theta^2\cos\phi^2 - 2C_{13}\tan\theta\cos\phi \tag{A15}$$

while B is calculated using

$$B = 2(C_{12} + C_{33}\tan\theta^2\sin\phi\cos\phi - \tan\theta(C_{13}\sin\phi + C_{23}\cos\phi)) \tag{A16}$$

and C is given by

$$C = C_{22} + C_{33}\tan\theta^2\sin\phi^2 - 2C_{23}\tan\theta\sin\phi \tag{A17}$$

The coefficients needed to find A, B, and C are

$$C_{11} = a^2\cos\psi^2 + \sin\psi^2(b^2\sin\delta^2 + \cos\delta^2) \tag{A18}$$

where δ is the angle the irregularities are inclined compared to the x-z plane, as defined in Figure 1. The required coefficients are

$$C_{22} = b^2\cos\delta^2 + \sin\delta^2 \tag{A19}$$

$$C_{33} = a^2\sin\psi^2 + \cos\psi^2(b^2\sin\delta^2 + \cos\delta^2) \tag{A20}$$

$$C_{12} = (b^2 - 1)\sin\psi\sin\delta\cos\delta \tag{A21}$$

$$C_{13} = (a^2 - b^2\sin\delta^2 - \cos\delta^2)\sin\psi\cos\psi \tag{A22}$$

The term ψ is the magnetic inclination at the IPP. This enables the Geometric factor G to be found as

$$G = \frac{ab}{\cos\theta\sqrt{AC - B^2\ /\ 4}} \tag{A23}$$

Finally, the expression for $\wp(p)$ is given by

$$\wp(p) = \frac{ab}{\sqrt{A''C^{(p/2)}}}F_2^1\left[(1-p)\ /\ 2, 1\ /\ 2 | (A'' - C'')\ /\ A''\right] \tag{A24}$$

with the hypergeometric function ${}_1F_2\left[\cdot\right]$.

$$A' = (A\cos\phi^2 + B\cos\phi\sin\phi + C\sin\phi^2)\cos\theta^2 \tag{A25}$$

$$B' = (B\cos(2\phi) + (C - A)\sin(2\phi))\cos\theta \tag{A26}$$

$$C' = A\sin\phi^2 - B\cos\phi\sin\phi + C\cos\phi^2 \tag{A27}$$

$$D' = \sqrt{(C' - A')^2 + B'^2} \tag{A28}$$

$$A'' = (A' + C' + D') / 2 \quad \text{(A29)}$$

$$C'' = (A' + C' - D') / 2 \quad \text{(A30)}$$

Data Availability Statement

ACE data are available via NASA data center (at https://cdaweb.gsfc.nasa.gov/index.html). SymH/Kp and AE are obtained from the Kyoto World Data Center for Geomagnetism (http://wdc.kugi.kyoto-u.ac.jp/). RISR-N data is available from the Madrigal database (http://isr.sri.com/madrigal). CHAIN data is available from the University of New Brunscwick (ftp://chain.physics.unb.ca/gps/data/nvd/) DISTRIBUTION STATEMENT A. Approved for public release; distribution is unlimited. Approved for Public Release 20-MDA-10561 (August, 31 2020).

Acknowledgments
The authors would like to acknowledge the use of SuperDARN data. SuperDARN is a collection of radars funded by national scientific funding agencies of Australia, Canada, China, France, Italy, Japan, Norway, South Africa, United Kingdom, and the United States of America. This material is based upon works supported by the Resolute Bay Observatory which is a major facility funded by the National Science Foundation through cooperative agreement AGS-1840962 to SRI International. The authors also wish to acknowledge the use of ACE data which is obtained from NASA's CDAWEB. The authors also wish to acknowledge Dr. Kathryn McWilliams at the University of Saskatchewan for the use of SuperDARN data. The authors also acknowledge all the guidance they received while completing this work. Kshitija Deshpande would like to acknowledge NSF CAREER grant AGS-1848207. AMDG.

References

Aarons, J. (1982). Global morphology of ionospheric scintillations. *Proceedings of the IEEE*, *70*(4), 360–378. https://doi.org/10.1109/proc.1982.12314

Akala, A. O., Doherty, P. H., Carrano, C. S., Valladares, C. E., & Groves, K. M. (2012). Impacts of ionospheric scintillations on GPS receivers intended for equatorial aviation applications. *Radio Science*, *47*(4), RS4007. https://doi.org/10.1029/2012RS004995

Baker, K. B., & Wing, S. (1989). A new magnetic coordinate system for conjugate studies at high latitudes. *Journal of Geophysical Research*, *94*(A7), 9139–9143. https://doi.org/10.1029/JA094iA07p09139

Basu, S., Groves, K., Basu, S., & Sultan, P. (2002). Specification and forecasting of scintillations in communication/navigation links: Current status and future plans. *Journal of Atmospheric and Solar-Terrestrial Physics*, *64*(16), 1745–1754. https://doi.org/10.1016/S1364-6826(02)00124-4

Beach, T. L., & Lovelace, R. V. E. (1997). Diffraction by a sinusoidal phase screen. *Radio Science*, *32*, 913–921. https://doi.org/10.1029/97RS00063

Briggs, B. H. (1975). Ionospheric irregularities and radio scintillations. *Contemporary Physics*, *16*(5), 469–488. https://doi.org/10.1080/00107517508210825

Carlson, H. C. (2012). Sharpening our thinking about polar cap ionospheric patch morphology, research, and mitigation techniques. *Radio Science*, *47*(4), RS0L21. https://doi.org/10.1029/2011RS004946

Carrano, C. (2012). *Ionospheric propagation effects on GNSS satellite signals*. ESA ESAC.

Carrano, C., Valladares, C., & Groves, K. (2012). Latitudinal and local time variation of ionospheric turbulence parameters during the conjugate point equatorial experiment in Brazil. *International Journal of Geophysics*, *16*. https://doi.org/10.1155/2012/103963

Carrano, C. S., Groves, K. M., & Caton, R. G. (2012). Simulating the impacts of ionospheric scintillation on L band SAR image formation. *Radio Science*, *47*(4), RS0L20. https://doi.org/10.1029/2011RS004956

Carrano, C. S., Groves, K. M., Rino, C. L., & Doherty, P. H. (2016). A technique for inferring zonal irregularity drift from single-station GNSS measurements of intensity (S_4) and phase (σ_ϕ) scintillations. *Radio Science*, *51*(8), 1263–1277. https://doi.org/10.1002/2015rs005864

Carrano, C. S., & Rino, C. L. (2019). Irregularity parameter estimation for interpretation of scintillation doppler and intensity spectra. In *2019 United States National Committee of URSI National Radio Science Meeting (USNC-URSI NRSM)* (p. 1–2). IEEE. https://doi.org/10.23919/USNC-URSI-NRSM.2019.8713120

Cervera, M. A., & Thomas, R. M. (2006). Latitudinal and temporal variation of equatorial ionospheric irregularities determined from GPS scintillation observations. *Annales Geophysicae*, *24*(12), 3329–3341. https://doi.org/10.5194/angeo-24-3329-2006

Collin, R. E. (1985). *Antennas and radiowave propagation*. McGraw-Hill Series in Electrical Engineering.

Crowley, G. (1996). Critical review of ionospheric patches and blobs. *Review of Radio Science 1993–1996*, 619–648.

Dandekar, B. S., & Groves, K. M. (2004). Using ionospheric scintillation observations for studying the morphology of equatorial ionospheric bubbles. *Radio Science*, *39*(3), RS3010. https://doi.org/10.1029/2003RS003020

De Franceschi, G., Alfonsi, L., Romano, V., Aquino, M., Dodson, A., Mitchell, C., et al. (2008). Dynamics of high-latitude patches and associated small-scale irregularities during the October and November 2003 storms. *Journal of Atmospheric and Solar-Terrestrial Physics*, *70*, 879–888. https://doi.org/10.1016/j.jastp.2007.05.018

Deshpande, K. B., Bust, G. S., Clauer, C. R., Rino, C. L., & Carrano, C. S. (2014). Satellite-beacon Ionospheric-scintillation global model of the upper Atmosphere (SIGMA) I: High-latitude sensitivity study of the model parameters. *Journal of Geophysical Research: Space Physics*, *119*(5), 4026–4043. https://doi.org/10.1002/2013JA019699

Deshpande, K. B., Bust, G. S., Clauer, C. R., Scales, W. A., Frissell, N. A., Ruohoniemi, J. M., & Weatherwax, A. T. (2016). Satellite-beacon Ionospheric-scintillation Global Model of the upper Atmosphere (SIGMA) II: Inverse modeling with high-latitude observations to deduce irregularity physics. *Journal of Geophysical Research: Space Physics*, *121*(9), 9188–9203. https://doi.org/10.1002/2016JA022943

Dierendonck, A. V., Klobuchar, J., & Hua, Q. (1993). Ionospheric scintillation monitoring using commercial single frequency C/A code receivers. In *Proceedings of the 6th International Technical Meeting of the Satellite Division of the Institute of Navigation* (pp. 1333–1342).

Gaussiran, T., Munton, D., Harris, B., & Tolman, B. (2004). An open source toolkit for GPS processing, total electron content effects, measurements and modeling. In *International Beacon Satellite Symposium 2004*.

Heinselman, C. J., & Nicolls, M. J. (2008). A Bayesian approach to electric field and E-region neutral wind estimation with the poker flat advanced modular incoherent scatter radar. *Radio Science*, *43*(5), RS5013. https://doi.org/10.1029/2007RS003805

Hosokawa, K., Shiokawa, K., Otsuka, Y., Ogawa, T., St-Maurice, J.-P., Sofko, G. J., & Andre, D. A. (2009). Relationship between polar cap patches and field-aligned irregularities as observed with an all-sky airglow imager at Resolute Bay and the PolarDARN radar at Rankin Inlet. *Journal of Geophysical Research*, *114*(A3), A03306. https://doi.org/10.1029/2008JA013707

Humphreys, T. E., Psiaki, M. L., Hinks, J. C., O'Hanlon, B., & Kintner, P. M. (2009). Simulating ionosphere-induced scintillation for testing GPS receiver phase tracking loops. *IEEE Journal of Selected Topics in Signal Processing*, *3*(4), 707–715.
Jayachandran, P. T., Langley, R. B., MacDougall, J. W., Mushini, S. C., Pokhotelov, D., Hamza, A. M., & Carrano, C. S. (2009). Canadian high arctic ionospheric network (CHAIN). *Radio Science*, *44*(01), RS0A03. https://doi.org/10.1029/2008RS004046
Jiao, Y., Morton, Y., Taylor, S., & Pelgrum, W. (2013). Characterization of high-latitude ionospheric scintillation of GPS signals. *Radio Science*, *48*(6), 698–708. https://doi.org/10.1002/2013RS005259
Jiao, Y., & Morton, Y. T. (2015). Comparison of the effect of high-latitude and equatorial ionospheric scintillation on GPS signals during the maximum of solar cycle 24. *Radio Science*, *50*(9), 886–903. https://doi.org/10.1002/2015RS005719
Jin, Y., Moen, J. I., & Miloch, W. J. (2014). GPS scintillation effects associated with polar cap patches and substorm auroral activity: Direct comparison. *Journal of Space Weather and Space Climate*, *4*.
Jin, Y., Moen, J. I., & Miloch, W. J. (2015). On the collocation of the cusp aurora and the GPS phase scintillation: A statistical study. *Journal of Geophysical Research: Space Physics*, *120*(10), 9176–9191. https://doi.org/10.1002/2015JA021449
Kelley, M. C., Vickrey, J. F., Carlson, C. W., & Torbert, R. (1982). On the origin and spatial extent of high-latitude F region irregularities. *Journal of Geophysical Research*, *87*(A6), 4469–4475. https://doi.org/10.1029/JA087iA06p04469
Kintner, P. M., Ledvina, B. M., & de Paula, E. R. (2007). GPS and ionospheric scintillations. *Space Weather*, *5*(9), S09003. https://doi.org/10.1029/2006SW000260
Knepp, D. L. (1983). Multiple phase-screen calculation of the temporal behavior of stochastic waves. *Proceedings of the IEEE*, *71*(6), 722–737. https://doi.org/10.1109/PROC.1983.12660
Knepp, D. L. (2016). Multiple phase screen calculation of two-way spherical wave propagation in the ionosphere. *Radio Science*, *51*(4), 259–270. https://doi.org/10.1002/2015RS005915
Knepp, D. L., & Reinking, J. T. (1989). Ionospheric environment and effects on space-based radar detection. In L. J. Cantafio (Ed.), *Spaced-based radar handbook*. Artech House Inc.
Lamarche, L. J., & Makarevich, R. A. (2017). Radar observations of density gradients, electric fields, and plasma irregularities near polar cap patches in the context of the gradient-drift instability. *Journal of Geophysical Research: Space Physics*, *122*(3), 3721–3736. https://doi.org/10.1002/2016JA023702
Laundal, K. M., & Richmond, A. D. (2017). Magnetic coordinate systems. *Space Science Reviews*, *206*(1), 27–59. https://doi.org/10.1007/s11214-016-0275-y
Lovelace, R. V. E., Salpeter, E. E., Sharp, L. E., & Harris, D. E. (1970). Analysis of observations of interplanetary scintillations. *The Astrophysical Journal*, *159*.
Marchenko, N. (2014). Northern sea route: Modern state and challenges. Paper presented at *International Conference on Offshore Mechanics and Arctic Engineering, Volume 10: Polar and Arctic Science and Technology, 10*.
Morton, Y., Bourne, H., Carroll, M., Jiao, Y., Kassabian, N., Taylor, S., et al. (2014). Multi-constellation GNSS observations of equatorial ionospheric scintillation. In *2014 XXXIth URSI General Assembly and Scientific Symposium (URSI GASS)* (p. 1–4). https://doi.org/10.1109/URSIGASS.2014.6929773
Oksavik, K., van der Meeren, C., Lorentzen, D. A., Baddeley, L. J., & Moen, J. (2015). Scintillation and loss of signal lock from poleward moving auroral forms in the cusp ionosphere. *Journal of Geophysical Research: Space Physics*, *120*(10), 9161–9175. https://doi.org/10.1002/2015JA021528
Paznukhov, V. V., Carrano, C. S., Doherty, P. H., Groves, K. M., Caton, R. G., Valladares, C. E., et al. (2012). Equatorial plasma bubbles and L-band scintillations in Africa during solar minimum. *Annales Geophysicae*, *30*(4), 675–682. https://doi.org/10.5194/angeo-30-675-2012
Press, W. H., Flannery, B. P., Teukolsky, S. A., & Vetterling, W. T. (1992). *Numerical recipes in C: The art of scientific computing* (2nd ed.). Cambridge University Press.
Rino, C. L. (1979). A power law phase screen model for ionospheric scintillation: 1. Weak scatter. *Radio Science*, *14*(6), 1135–1145. https://doi.org/10.1029/RS014i006p01135
Rino, C. L., & Fremouw, E. J. (1977). The angle dependence of singly scattered wavefields. *Journal of Atmospheric and Terrestrial Physics*, *39*(8), 859–868.
Rino, C. L., Livingston, R. C., & Matthews, S. J. (1978). Evidence for sheet-like auroral ionospheric irregularities. *Geophysical Research Letters*, *5*(12), 1039–1042. https://doi.org/10.1029/GL005i012p01039
Rino, C. L., & Owen, J. (1980). The time structure of transionospheric radio wave scintillation. *Radio Science*, *15*(3), 479–489. https://doi.org/10.1029/RS015i003p00479
Rufenach, C. L. (1974). Wavelength dependence of radio scintillation: Ionosphere and interplanetary irregularities. *Journal of Geophysical Research*, *79*(10), 1562–1566. https://doi.org/10.1029/JA079i010p01562
Taylor, S., Morton, Y., Marcus, R., Bourne, H., Pelgrum, W., & Dierendonck, A. V. (2013). High-latitude irregularity spectra deduced from scintillation measurements. In *Proceedings of the ION 2013 Pacific PNT Meeting* (pp. 743–751). Retrieved from https://www.ion.org/publications/abstract.cfm?ArticleID=11036
Thayer, J. P., & Semeter, J. (2004). The convergence of magnetospheric energy flux in the polar atmosphere. *Journal of Atmospheric and Solar-Terrestrial Physics*, *66*(10), 807–824. https://doi.org/10.1016/j.jastp.2004.01.035
Thébault, E., Finlay, C. C., Beggan, C. D., Alken, P., Aubert, J., Barrois, O., et al. (2015). International geomagnetic reference field: The 12th generation. *Earth Planets and Space*, *67*(1), 79.
Wernik, A. W., Liu, C. H., Franke, S. J., & Gola, M. (1990). High-latitude irregularity spectra deduced from scintillation measurements. *Radio Science*, *25*(5), 883–895. https://doi.org/10.1029/RS025i005p00883
Yeh, K. C., & Liu, C.-H. (1982). Radio wave scintillations in the ionosphere. *Proceedings of the IEEE*, *70*(4), 324–360.
Zettergren, M., Semeter, J., & Dahlgren, H. (2015). Dynamics of density cavities generated by frictional heating: Formation, distortion, and instability. *Geophysical Research Letters*, *42*, 10120–10125. https://doi.org/10.1002/2015GL066806
Zhang, Q., Zhang, B., Moen, J. I., Lockwood, M., McCrea, I. W., Yang, H., et al. (2013). Polar cap patch segmentation of the tongue of ionization in the morning convection cell. *Geophysical Research Letters*, *40*(12), 2918–2922. https://doi.org/10.1002/grl.50616